Research Square

Preprints are preliminary reports that have not undergone peer review.
They should not be considered conclusive, used to inform clinical practice,
or referenced by the media as validated information.

Design Assessment and Test of Compact Gyroid-tpms Heat Exchanger With Embedded Coolant Channels for Ltpem Fuel Cell Powered Regional Aircraft

Chetan Sain

chetan.sain@dlr.de

German Aerospace Center

Akilan Mathiazhagan

Brandenburg University of Technology Cottbus-Senftenberg

Sahil Bhapkar

German Aerospace Center

Majid Asli

Brandenburg University of Technology Cottbus-Senftenberg

Klaus Höschler

Brandenburg University of Technology Cottbus-Senftenberg

Stefan Kazula

German Aerospace Center

Research Article

Keywords:

Posted Date: May 20th, 2026

DOI: https://doi.org/10.21203/rs.3.rs-9416182/v1

License: This work is licensed under a Creative Commons Attribution 4.0 International License.
Read Full License

Additional Declarations: No competing interests reported.

DESIGN ASSESSMENT AND TEST OF COMPACT GYROID-TPMS HEAT EXCHANGER WITH EMBEDDED COOLANT CHANNELS FOR LTPEM FUEL CELL POWERED REGIONAL AIRCRAFT

Chetan Sain[1], Akilan Mathiazhagan[2], Sahil Bhapkar[1], Majid Asli[2], Klaus Höschler[2], Stefan Kazula[1]

[1] Institute of Electrified Aero Engines, German Aerospace Center, Cottbus, Germany
[2] Chair of Aero Engine Design, Brandenburg University of Technology Cottbus-Senftenberg, Germany

Abstract

All-electric aircraft with fuel cell-powered propulsion are considered a key technology for enabling low-emission flights. However, the feasibility of fuel cell systems for regional flights is challenging because their current mass-specific power densities are lower than required. Heat exchangers (HEXs) are critical component which are necessary for the cooling of fuel cell stacks, power electronics and pre-conditioning of fuel. HEXs must be designed lightweight to improve the power density of the propulsion system and compact for easy integration and drag reduction. Among several existing types of HEXs, designs based on Triply Periodic Minimal Surface (TPMS) geometries are used for compact HEXs. This paper introduces a compact gyroid-pipe HEX, designed using TPMS gyroid surfaces and with integrated coolant channels. Three design variants of gyroid-pipe HEX with thickness of 20 mm, 30 mm and 40 mm are generated using TPMS unit cell aspect ratio (AR) of 1, 1.5 and 2 respectively. Thermal-hydraulic performance is calculated using Computational Fluid Dynamics (CFD) simulations on small periodic cells, denoted simply as AR1, AR1.5 and AR2 with their respective above-mentioned thicknesses. Results show that with increasing ARs, pressure losses reduce, improving the hydraulic performance but the thermal performance decreases. Prototypes with a frontal cross-section of 200 mm x 200 mm are developed using additive manufacturing with ARs of 1, 1.5 and 2. Experiments are conducted to measure the pressure drop across the air side of the HEX segments, denoted as AR1, AR1.5 and AR2. Eight additional combinations of AR1, AR1.5 and AR2 HEX segments are assembled to test the effect of compactness variation (increasing or decreasing compactness along the air side) on pressure drop measurements. The best result is achieved with a combination of AR2 and AR1.5 HEX segments (denoted AR2-AR1.5), where the AR2 segment with lower compactness is attached to the AR1.5 segment with higher compactness and facing the air inflow. This HEX configuration delivers a 3% reduction in pressure drop and pumping power while increasing the heat transfer surface area by a factor of 3.12 relative to the AR1 configuration, without altering the frontal area or mass flow rate. Hence, it is a potential candidate for future studies and thermal tests. Structural calculations are performed to estimate the stiffness and thermal conductivity matrices for the AR1, AR1.5 and AR2 segments. Using these characteristics, a stress assessment is performed on all the ARs and their eight additional combinations at different angles of inclination inside the air duct. The results reveal that, while AR1 and AR1.5 are reliable options individually, especially at higher inclinations, Combinations of all three ARs offer the most favorable structural performance across all angles of inclination. This makes them the strongest candidates for integration and structural testing in future studies. The methodologies used in this paper for the thermal, hydraulic and structural assessment of the TPMS gyroid pipe HEX will be validated using further experiments.

1. INTRODUCTION

Achieving low-emission flights is the aim of the Flightpath 2050 and Waypoint 2050 strategies, and this can be achieved through all-electric aircraft propulsion powered by carbon-free fuels such as gaseous hydrogen [1]. In an all-electric propulsion system, energy is generated by fuel cells or batteries. LTPEM fuel cells are one type of fuel cell; they are approximately 50% efficient, meaning half of the energy is lost in the form of heat. A heat exchanger (HEX) is a critical component of the thermal management system, necessary for dissipating excess heat out of the propulsion system. However, for a regional aircraft, powered by an LTPEM fuel cell system, the HEX can be too heavy and bulky to be integrated into the system [2]. Therefore, it must be designed to be as compact and lightweight as possible, forming an integral part of the propulsion system. TPMS geometries offer a large surface-to-volume ratio and are utilized to create compact HEXs with high performance [3] [4]. Key functions of a HEX in LTPEM fuel cell system include dissipating excess heat from the LTPEM coolant loop while maintaining its temperature difference with the least possible drag and the power consumption. Air-cooled HEXs are ideal for aircraft as air is available as a heat sink during flight. However, in general, air-cooled HEXs are large due to the lower specific heat capacity of air compared to liquid coolants. In order to maintain a high heat transfer rate, the air mass flow rate and the air-wetted heat transfer surface area inside the HEX core must be large. The heat transfer surface area is increased using compact HEXs without exceeding the design domain volume. With air as a cooling medium, HEX compactness of 700 mm^2/mm^3 and above is categorized as a compact HEX [5]. With higher compactness, a passive air flow is not sufficient to overcome the resistance inside the narrow channels of the compact HEX. An additional air blower or compressor is necessary to overcome the pressure and deliver the required large air mass flow rates. The power consumption by compressor is known as pumping power, which should be minimized in order to reduce the mass and fuel burn penalties linked to a large compressor [6].

This paper introduces a compact HEX design based on gyroid TPMS geometry with embedded coolant channels in its wall structure. This design is denoted as a 'gyroid-pipe

HEX'. To the authors' knowledge, there are no TPMS-based HEXs with altered geometry, such as embedded coolant channels, in the open literature, nor are there any experimental results. The research question addressed in this paper is to study the design and performance of the compact gyroid-pipe HEX, and to quantify the effects of variable compactness on the thermal, hydraulic, and structural properties using three design variants.

The next chapter outlines the design of the gyroid-pipe HEX and its three variants. This is followed by an explanation of the methodology and presentation of the results of the thermal-hydraulic performance assessment. After that, there is a brief description of the experimental setup and the results of the pressure drop test. Chapters 5 and 6 describe the methodology and results of the structural assessment of the gyroid-pipe design variants and their orientations inside the air duct. The final chapters provide a conclusion and an outlook on further studies.

2. DESIGN DEVELOPMENT OF GYROID-PIPE HEX

TPMS geometries are mathematically driven three-dimensional periodic surfaces with zero mean curvature [7]. In a HEX, these geometries can be used to increase the heat transfer surface area within a given unit volume. The ratio of the heat transfer surface area to its enclosed volume is known as HEX compactness. TPMS geometries enable a HEX to have a high level of compactness and increase its heat transfer capacity, which can be comparatively higher than that of conventional HEX designs [3] [4] [7] [8]. Of the various TPMS geometries, the gyroid is a common type that provides a three-dimensional continuous surface without allowing an abrupt change in flow direction. FIGURE 1 shows the steps applied to design the gyroid-pipe HEX using TPMS gyroid unit cells and integrated coolant pipes. The following implicit equation (1) for gyroid is used in Python to create splines inside a 10 mm cube, as shown in FIGURE 1a.

$$cos(x).sin(y) + cos(y).sin(z) + cos(z).sin(x) = 0 \quad (1)$$

These splines are imported into NX software[1], a 3D CAD software program, to model the gyroid surfaces. As illustrated in FIGURE 1b, two gyroid units are patterned at each end, creating a thin-walled gyroid unit cell with an edge length of 10 mm. The paths of the embedded coolant channels along the gyroid curvatures are indicated by the splines in FIGURE 1b and FIGURE 1c.

Due to its aerodynamic shape and tolerable angles for additive manufacturing, oval cross-section has been selected for the coolant channels. The channels are arranged in rows in a cross-flow configuration relative to the air flow. The small unit shown in FIGURE 1c is patterned along a 200 mm x 200 mm cross-section to create the gyroid-pipe HEX segment shown in FIGURE 1d. This segment's core consists of 800 unit cells, resulting in 39 pairs of parallel coolant channels arranged in a cross-flow configuration. The length of the HEX segment is kept variable, with three design variants developed as described in the next section.

This paper assesses the design of three different variations to study their effect on aero-thermal performance and structural characteristics. As illustrated in FIGURE 2, the TPMS gyroid unit cells are stretched along the air side length at aspect ratios of 1, 1.5 and 2, with a constant width of 10 mm. TAB 1 lists the dimensions of the key design parameters for all three variants. These design variants of the gyroid pipe HEX are subsequently denoted as AR1, AR1.5 and AR2.

As ARs increase, so does pore size. This indicates that the smallest effective cross-section within the air domain is increasing, which would increase the air mass flow rate. Porosity ϵ is defined as the ratio of void volume to unit cell volume. As the AR grows, both factors change to a similar extent, so the $\epsilon = 62\%$ for AR1, AR1.5 and AR2. Stretching the unit cell from AR1 to AR1.5 and AR2 changes the pitch, amplitude, mass and volume of the air, coolant and solid structure by a similar factor of 1.5 or 2. A higher amplitude indicates greater curvature along the air side, which influences the flow characteristics. This is not true of surface area variation. The air wetted and coolant wetted surface areas increase by 37.7% and 43%, respectively, when the design changes from AR1 to AR1.5, and by 43% and 87.2%, respectively, when the design changes from AR1 to AR2. The volume varies more than the surface area, which decreases the compactness of the unit cell. As shown in TAB 1, the compactness of the air domain reduces by 8.1% and 11.5% with AR1.5 and AR2, respectively, compared to AR1. The width of the coolant channels increases, but the height of the channels remains constant at 1.8 mm. With higher ARs, the curvatures of the coolant channels increase along their flow direction, and the influence of this is studied in this research. The aim of this paper is to study the effects of the above-mentioned design parameters on the thermal-hydraulic and structural characteristics of the gyroid-pipe HEX. The following chapter describes the thermal-hydraulic assessment methodology and post-processing using CFD simulations.

Parameter	Unit	AR1	AR1.5	AR2
Aspect ratio	-	1	1.5	2
Length	mm	20	30	40
Pitch	mm	5	7.5	10
Amplitude	mm	2.3	3.5	4.6
Wall thickness	mm	0.5	0.75	1
Pore diameter	mm	1.94	2.14	2.26
Mass	g	0.505	0.757	1.01
Air-wetted area	mm^2	1258	1732	2226
Compactness	m^2/m^3	1013	930	896
Channel width	mm	3.71	5.56	7.42
Coolant wetted area	mm^2	391	560	732

TAB 1. Key design parameters of gyroid-pipe unit cell with AR1, AR1.5, AR2.

[1] Siemens Industries Digital Software. NX, 2024

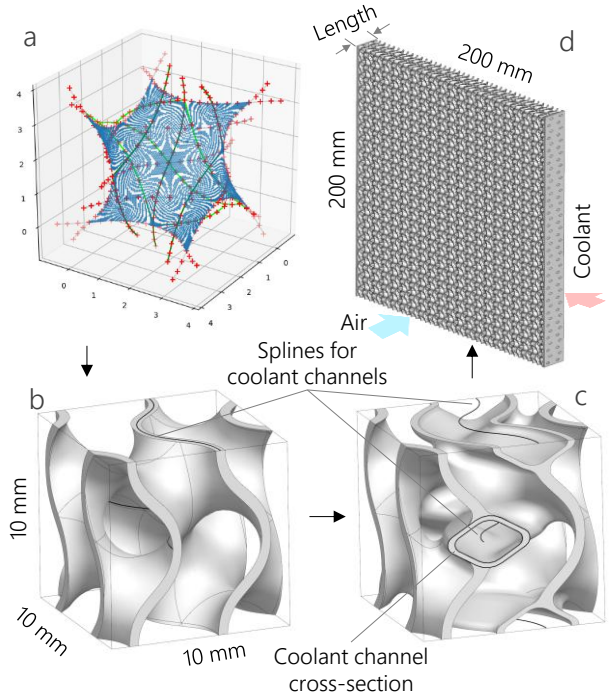

FIGURE 1 Design workflow of gyroid-pipe unit cell to HEX prototype.

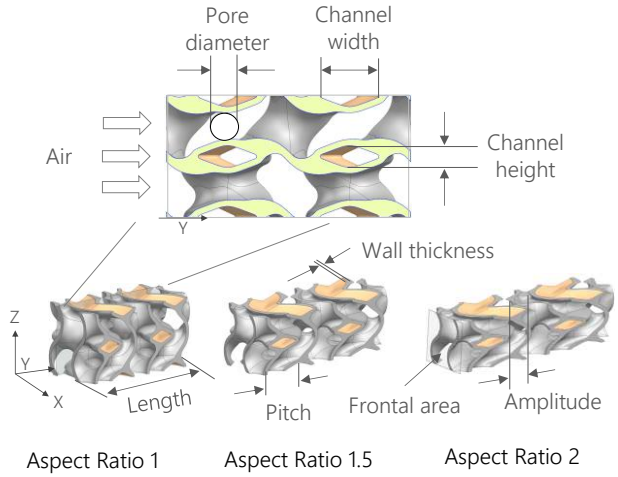

FIGURE 2 TPMS gyroid-pipe periodic cells with aspect ratio 1, 1.5, and 2 (bottom) and 2D cross-section (top) with key design parameters.

3. THERMAL-HYDRAULIC ASSESSMENT

In general, correlations from experiments are available in literature for performance estimation for most of the known types of HEXs. However, for compact HEXs based on complex geometries such as TPMS, there are very few validated correlations for heat transfer and pressure drop [9–12]. No validated correlations are found for the gyroid sheet TPMS with altered designs, such as those with embedded coolant channels, as described above. In general, performance estimation can be achieved through CFD simulations. The setup and results of these simulations must be validated by experiments.

3.1. Methodology

This paper presents CFD simulations performed to predict the heat transfer and aerodynamic performance of the gyroid-pipe units AR1, AR1.5 and AR2. The CFD domains consist of air, liquid coolant and a solid gyroid pipe unit cell, as shown in FIGURE 3 for the AR1 design point.

The air domain contains an air inlet and an air outlet. The inlet velocity condition varies from 10 m/s to 30 m/s at 303.15 K and the outlet pressure is set to 101325 Pa. The air domain extends towards the inlet to ensure fully developed inflow in front of the unit cell structure, capturing the distorted flow caused by the leading edge thickness. Similarly, the outlet is extended to twice the length of the unit cell structure to sufficiently resolve turbulence and avoid the effects of backflow. The coolant domain consists of six individual bodies attached to the surfaces of the solid counterpart channels. The coolant channels on the top and bottom surfaces are halved as part of the periodic repeating unit cell structure. The coolant channels are extended towards their inlet and outlet planes, similar to the air domain, to ensure fully developed boundary layer flow and reduce back pressure effects. The velocity at the coolant inlets is fixed at 1 m/s and the temperature at 353.17 K, and an ambient pressure of 101325 Pa is set. A symmetry boundary condition is placed at all the top and bottom surfaces. Furthermore, a periodic flow condition is defined at all the side faces of the solid and air domains. On the surface of the solid domain wetted by coolant and air, a wall with a no-slip condition is defined. To enable heat transfer from the hot coolant through the solid unit cell body into the cold air, a coupled heat transfer condition is applied.

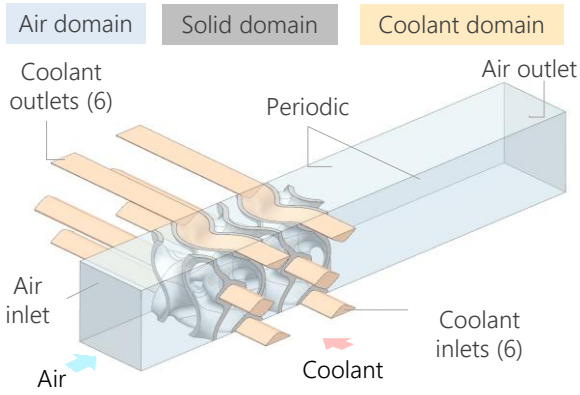

FIGURE 3 CFD domains and boundaries.

A computational mesh is generated using ANSYS Mesher[2], consisting of a hybrid mesh with tetrahedral elements sized at 0.1 mm in solids and 0.5 mm in fluids. To resolve the thermal and momentum boundary layer flow, at least 15 prism layers are created on the walls, with an average first layer height of 0.01 mm.

The material properties of air are taken from the ANSYS Fluent[3] database and are defined as follows: an ideal gas for density ρ_{air}, the Sutherland model for viscosity, and a polynomial function of temperature for specific heat capacity $C_{p,air}$ and thermal conductivity k_{air}. Water is used as the coolant, with a constant density of ρ_{water}= 998.2 kg/m³, a specific heat capacity of $C_{p,water}$= 4182 J/(kgK) and

[2] ANSYS Meshing, Release 2024 R1, ANSYS Inc.

[3] ANSYS Fluent, Release 2024 R1, ANSYS Inc.

thermal conductivity of k_{water} = 0.6 W/(mK). Aluminum is assigned to the solid domain with a density of ρ_{AL}= 2,719 kg/m³, a specific heat capacity of $C_{p,AL}$= 871 J/(kg K) and a thermal conductivity of k_{AL} = 202.4 W/(m K).

CFD simulations are carried out in steady-state using a 3D RANS density-based implicit solver in the ANSYS Fluent software package[4]. The inbuilt k-omega SST viscous model is applied to simulate turbulence and compressible flow. The convergence conditions are set as residuals for continuity, velocity, energy and turbulence under 10^{-7}, as well as a relative and constant change in mass flow rate and temperature under 10^{-3}. The aforementioned CFD setup and computational mesh are defined using best practice and validated approaches published in [13] [14].

Output from the CFD simulations is processed using key parameters which are briefly described as follows and with details in [5] [15–17].

Hydraulic diameter, D_h, for TPMS structures can be defined as:

$$D_h = \frac{4 \cdot \epsilon}{A_{sp}} \tag{2}$$

where the specific surface area A_{sp} is defined as the ratio of the air-wetted surface area to the volume of the HEX unit cell, while porosity ϵ is the fraction of the void volume inside the HEX unit cell.

The Reynolds number for the air flow through compact TPMS structures can be defined as a function of dynamic viscosity with υ_{air} = 1.81x10^{-5} Pa s, density, average velocity and D_h as:

$$Re = \frac{\rho_{air} \cdot V_{air} \cdot D_h}{\upsilon_{air}} \tag{3}$$

The Nusselt number, Nu, is a dimensionless parameter representing the ratio of convective heat transfer to effective molecular thermal conductance. It is defined in equation (4) as a function of the heat flux, q, the hydraulic diameter, D_h, the temperature difference between the air-wetted walls T_{wall} and the average bulk temperature $T_{air,bulk}$ of the air domain, and the effective thermal conductivity, $k_{eff,air}$ as:

$$Nu = \frac{q \cdot D_h}{(T_{wall} - T_{air,bulk}) \cdot k_{eff,air}} \tag{4}$$

T_{wall} and q are calculated from the CFD simulations as an area-weighted average of the surface integral on air-wetted surfaces. The $T_{air,bulk}$ and $k_{eff,air}$ are calculated as an average of the volume integral of the HEX air core domain.

Heat transfer coefficient, HTC defines the amount of heat transfer across per unit surface area and per unit temperature change. The HTC is calculated in equation (5) using the Nu, $k_{eff,air}$ and D_h, as follows:

$$HTC = \frac{Nu \cdot k_{eff,air}}{D_h} \tag{5}$$

The Colburn factor, j, is defined as a function of the HTC and Prandtl number, Pr. Pr defines the fluid property as the ratio of momentum diffusivity to thermal diffusivity. Momentum diffusivity is a function of the fluid's kinematic viscosity and represents the thickness of the boundary layer of the flow. Thermal diffusivity depends on the fluid's thermal conductivity and represents the thickness of the thermal boundary layer. Pr is an important dimensionless term used to account for heat transfer and the efficiency of the HEX. Pr is calculated as mass-weighted average in air CFD domain. The j factor is a dimensionless term that characterizes the rate of convective heat transfer relative to the rate of mass transport or the flow's momentum, as per equation (6). This factor can be used to compare different types of HEX for their thermal characteristics. It is defined as:

$$j = \frac{HTC \cdot Pr_{air}^{2/3}}{\rho_{air} \cdot V_{air} \cdot C_{p,air}} \tag{6}$$

The Fanning friction factor, f, is commonly used to quantify the hydraulic performance of the HEX core. Skin friction on surfaces that are wet with air and convective heat transfer from hot surfaces to the cold air boundary layer increase the specific energy of the air stream. This leads to a reduction in total pressure across the duct, in accordance with the law of conservation of energy [5]. In compact HEXs, the total pressure drop is primarily governed by entrance losses, momentum losses, core friction losses and exit losses. Core friction losses account for over 90% of the total loss [17]. The f-factor is widely used to describe this core friction loss. It is defined as the ratio of the core friction pressure drop to the dynamic pressure of the flow and represents the kinetic energy per unit volume, as per equation (7). In this study, core friction loss is quantified using CFD simulations. Mass-weighted averages of static and total pressure are obtained through surface integrals at the air inlet and outlet of the HEX core:

$$f = \frac{2 \cdot \Delta P \cdot D_h}{\rho_{air} \cdot V_{air}^2 \cdot L} \tag{7}$$

Pumping power is defined as the product of the pressure loss ΔP across the HEX core and the volume flow rate, as ratio of mass flow rate to density.

$$\text{Pumping power} = \frac{\dot{m} \cdot \Delta P}{\eta \cdot \rho} \tag{8}$$

Compressor efficiency is defined as η. This represents the input power required by a compressor or blower to pump the required air mass flow and overcome the pressure drop across the HEX. It is important to determine the friction characteristics of the air-wetted surface, since the pumping power requirement for the air side is much higher than for the liquid side due to the lower density of air and the higher mass flow requirement resulting from heat transfer with lower specific heat capacity [5].

3.2. Results

The thermal-hydraulic performance using the period gyroid-pipe element AR1, AR1.5 and AR2, as shown in FIGURE 2 is quantified using the aforementioned parameters. FIGURE 4 illustrates the f factor, j factor, HTC and ratio of

[4] ANSYS® Fluent®, Release 2024 R1, ANSYS, Inc.

j/f as surface goodness factor, representing thermal performance over the hydraulic performance.
As previously mentioned, the porosity remains the same for all three geometries (AR1, AR1.5 and AR2) at ϵ = 62.2%, resulting in D_h values of 3.8 mm, 4.2 mm and 4.4 mm, respectively. For the boundary condition with air inlet velocities ranging from 10 m/s to 30 m/s, the Re ranges from 1560 to 5560. This indicates that the flow regions inside the HEX unit cell mostly lie in the transition zone and at the lower end of fully turbulent flow. For the stretched cell with a higher AR, the Re is slightly higher by the same factor as the increase in D_h.

FIGURE 4a compares the f factors, equation (7), and shows that the AR2 achieves the lowest f factor, indicating superior hydraulic performance compared to AR1.5 and AR1 by a factor of 1.75 and 3.17, respectively. Core friction dominates the total pressure loss across the HEX, and geometric stretching of the unit cell from AR1 to AR1.5 and AR2 reduces this loss by an average of 33% and 48%, respectively. Increasing AR enlarges the flow passage hydraulic diameter (equation (2)), and decreases surface-to-volume ratio, which collectively reduce wall shear stresses and viscous energy dissipation, thereby lowering overall pressure drop. Although stretching the unit cell increases gyroid wall curvature, amplitude and pitch, these geometric changes improve flow alignment and reduce tortuosity, thereby mitigating frictional losses. As expected, total pressure drop increases with higher inlet velocities due to intensifying turbulence and frictional shear, yet the friction factor decreases with velocity (FIGURE 4a) because the increase in flow kinetic energy outpaces the rise in viscous losses. Furthermore, the slope of the friction factor curve decreases with increasing AR, indicating that higher-AR designs are less sensitive to velocity changes and thus provide enhanced hydraulic efficiency across a broader operating range.

FIGURE 4d shows the HTC for all three designs in relation to increasing air velocity. In general, HTC represents the heat transfer capability of a HEX per unit of surface area and temperature difference due to heat transfer, as per equation (5). Through HTC, different types, and sizes of HEX are compared for their thermal performance [5]. HTC increases with air velocity, demonstrating the highest heat transfer capability with AR1. On average, this is 17% higher than AR1.5 and 29% higher than AR2. Simulations show that moving from AR1 to AR2 (increasing D_h) results in an elevated difference between the T_{wall} and the $T_{air,bulk}$ and a decrease in $k_{eff,air}$ which reduces HTC. This can be explained as follows. As mentioned above, as the gyroid pitch becomes greater on the air side, the coolant channels bend with greater curvatures. This causes local regions of reverse coolant flow to grow, resulting in a longer retention time for the hot coolant. Consequently, the T_{wall} of air-wetted surfaces increases to a greater extent than the small rise in $T_{air,bulk}$. Additionally, the $k_{eff,air}$ decreases more dominantly with greater ARs.

FIGURE 4b shows the corresponding j factors for the three designs across the same range of flow velocities. Although HTC increases with velocity, the j factors decrease for all ARs, which is consistent with their dependence on HTC, the Pr and momentum transport, as per equation (6). At higher Re turbulence intensifies both momentum and thermal transport. However, eddy viscosity increases more rapidly than eddy thermal diffusivity, resulting in momentum transport outpacing heat transfer [5]. This imbalance results in the decline of j factors observed with increasing velocity. Furthermore, the reduction in HTC with higher ARs leads to a corresponding decrease in j factors among the three design variants, as per equation (6).

The combined thermal-hydraulic performance of a HEX is quantified using the surface goodness factor j/f, as shown in FIGURE 4c. This shows how effective the heat transfer surface is in terms of heat dissipation relative to frictional and pressure losses. The AR2 results in the highest j/f factors, exceeding the AR1 by an average of 2.35 times and the AR1.5 by 1.43 times. The reduction in pressure drop achieved by stretching the unit cells in the air direction has a dominant effect here. The sensitivity of the AR to pressure drop is examined further through experimental tests. A brief overview of the test setup and methodology is provided in the next chapter.

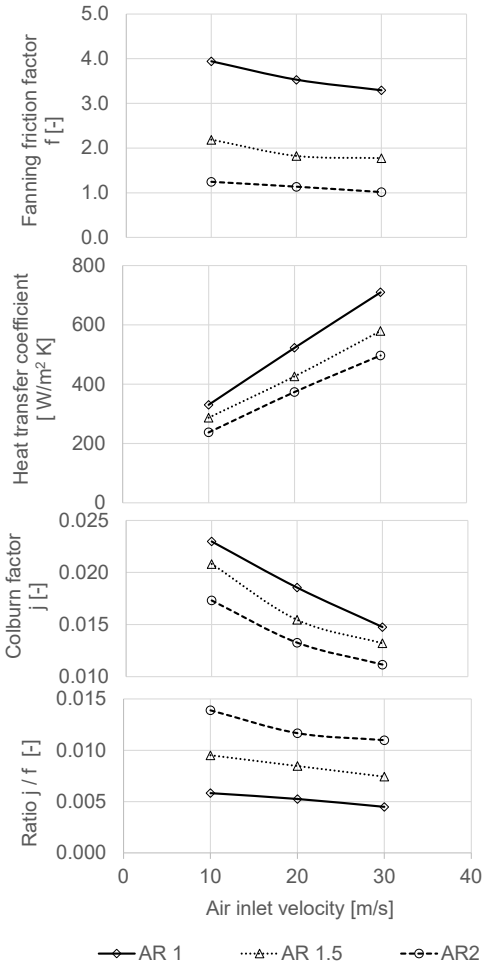

FIGURE 4 Thermal and hydraulic performance parameters for gyroid-pipe AR1, AR1.5 and AR2.

4. PRESSURE DROP MEASUREMENT USING EXPERIMENTS

This section provides a brief description of the experimental setup. Designed for pressure drop testing in the air domain only, the setup consists of air inlet ducts, a test section with integrated HEX segments, and pressure difference

sensors, as shown in FIGURE 5. The air inlet ducts have the same 200 mm x 200 mm cross-section as the HEX segments. Four small holes are drilled, one on each side of the duct and centered in front of and behind the HEX flow. Pressure measurement tubes are placed through these holes and both sides are connected to a pressure difference sensor. The front face of the inlet duct is connected to the air supply unit. Air is supplied externally through a wind tunnel under ambient room conditions. Three prototypes of the gyroid-pipe HEX with AR1, AR1.5 and AR2 are produced using 3D additive manufacturing. They have a uniform cross-section of 200 mm x 200 mm, as illustrated in FIGURE 1, and their respective lengths are 20 mm, 30 mm and 40 mm. Thermoplastic is selected as the material, and the fused filament fabrication technique is used to print the HEX prototype segments, as shown in FIGURE 5.

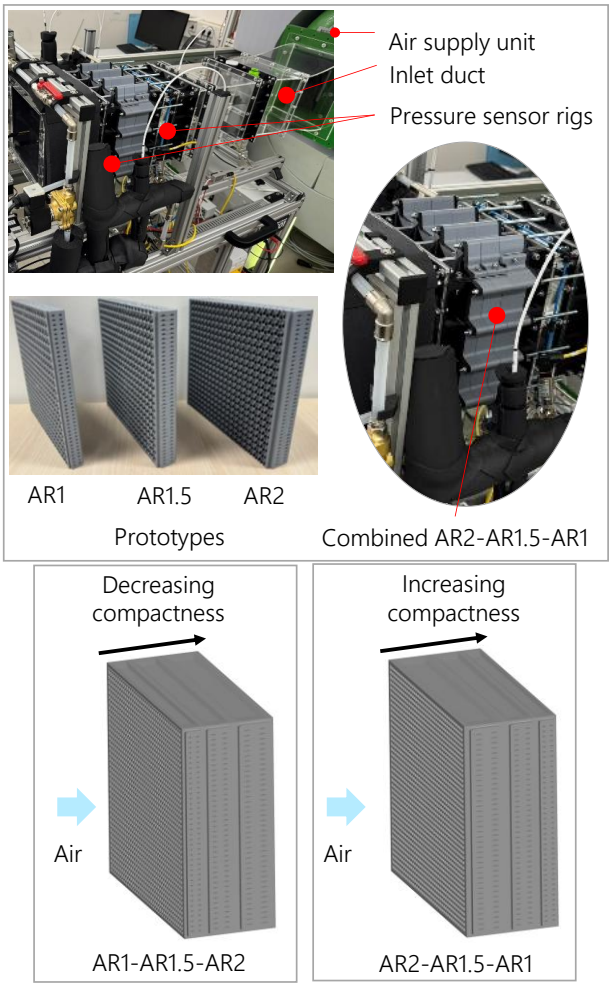

FIGURE 5 Experimental setup for pressure drop test with gyroid-pipe HEX, 3D printed prototypes (top) and examples combined configuration (bottom).

Configuration name	Length	Normalized area	Normalized mass flow rate	Normalized pumping power
	mm	-	-	-
AR1	20	1	1	1
AR1.5	30	1.37	1.031	0.600
AR2	40	1.75	0.986	0.412
AR1-AR1.5	50	2.37	1.016	1.578
AR1.5-AR1	50	2.37	1.014	1.604
AR1.5-AR2	70	3.12	1.001	0.975
AR2-AR1.5	70	3.12	1.001	0.970
AR1-AR2	60	2.75	1.025	1.484
AR2-AR1	60	2.75	0.998	1.444
AR1-AR1.5-AR2	90	4.12	1.005	2.009
AR2-AR1.5-AR1	90	4.12	1.015	2.034

TAB 2. HEX test configurations and results normalized to AR1 for air velocity 15 m/s.

The test involves increasing the air inflow speed from 1 m/s to 30 m/s in 60 steps. Five measurements of the pressure difference and air velocity are captured for each step. The average of these is taken as one data point. The tests are performed at room temperature. Eleven different configurations are tested; these are listed in TAB 2. In addition to single HEX segments, eight different combinations are assembled and tested. These combined configurations are denoted by their individual names and in the order of their appearance with respect to air flow direction. FIGURE 5 shows two examples, with combinations of all three ARs in increasing and decreasing order of compactness (AR2-AR1.5-AR1 and AR1-AR1.5-AR2, respectively). In configuration AR2-AR1.5-AR1, for example, the flow enters through the AR2 segment, passes through the AR1.5 segment, and then through the AR1 segment towards the outlet. All test configurations have no change in frontal cross-section area, and tests are performed under similar room and air supply conditions.

The test results are plotted in FIGURE 6 as the pressure drop in relation to the average air velocity. Considering air velocity of 15 m/s as the design operating point for the HEX performance and AR1 as the baseline design, normalized values for heat transfer surface area, air mass flow rate and pumping power are listed in TAB 2. As mentioned in an earlier chapter, pumping power is calculated as a function of the pressure drop multiplied by the mass flow rate and divided by the air density. Pumping power indicates the amount of power required to overcome pressure loss and enable the required volume flow rate in the HEX system. It should be as low as possible to improve the overall economic efficiency of the HEX system[5] [14] [17].

The results shown in FIGURE 6 illustrate that the pressure drop across the gyroid pipe increases with rising air velocity. Dynamic pressure is also correlated with velocity in a quadratic manner. As AR increases, the pore diameter and pitch increase and the effective cross-section for airflow through the gyroid passages increases, meaning reduced blockage. This is measured in terms of the dynamic pressure difference between the inlet and the HEX outlet, which decreases. This results in a total pressure reduction, which, as can be seen in FIGURE 6, is smaller with higher ARs.

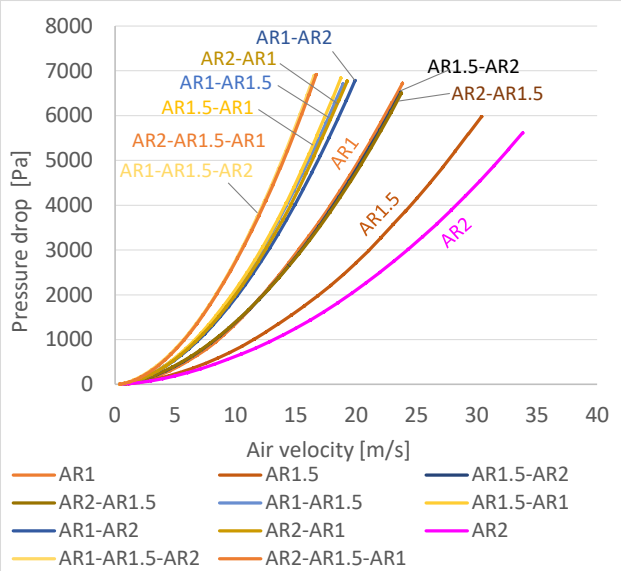

FIGURE 6 Pressure drop at air side for all test configurations.

The lowest pressure drop is measured with AR2 across entire velocity range, followed by AR1.5. The relative difference from AR1 increases with higher air velocities, indicating reduced flow blockage due to a larger effective cross-section and reduced form drag. The biggest gain is a 40% reduction in pumping power with AR1.5 and a 59% reduction with AR2, relative to AR1. On the downside, the structural mass is multiplied by factors of approximately 1.5 and 2, respectively, as listed in TAB 2.

The configurations AR2-AR1.5 and AR1.5-AR2 produced preferable results, showing slightly better hydraulic performance than the baseline AR1 configuration, with a similar mass flow rate. However, the drawback is that they are 3.46 times heavier. The pumping power is reduced by 3% and 2.5%, respectively, and both configurations result in a surface area that is 3.12 times larger, with a length of 70 mm. Due to the larger heat transfer surface area and the same mass flow rate, frontal area and flow rate, a higher thermal performance can be achieved than with AR1 without generating additional pumping power. These combinations have double the number of coolant channels, enabling greater heat transfer between a higher volume of hot coolant and increasing the temperature difference between the hot coolant and the cold air domain.

In the rest of the combined configuration involving AR1, greater pressure loss and, consequently, greater pumping power are measured. The combination of AR1 and AR2 delivers 2.75 times the heat transfer surface area of the baseline, but with 1.46 times the pumping power on average. The combination of AR1-AR1.5-AR2, where HEX porosity along the airflow direction increases, results in a 4.12-fold enhancement in surface area, though it comes with a cost: a doubling of pumping power, as shown in TAB 2. A comparable outcome is seen in the configuration AR2-AR1.5-AR1, where porosity decreases, yet the flow rate and pumping power remain slightly higher.

5. STRUCTURAL ASSESSMENT METHODOLOGY

Structural analysis of HEXs integrated within aircraft duct regions has gained importance due to the combined effects of pressure gradients, vibrational loading, and aerodynamic stresses during operation [18]. With additive manufacturing enabling novel compact HEXs based on TPMS architectures, structural modeling has become even more complex, as the intricate geometries demand extremely fine discretization for reliable predictions [19] [20]. Conducting full-scale finite element simulations of these architectures is computationally expensive, but their adoption highlights the need to understand stress distributions. This complexity underscores the opportunity for advanced modeling strategies to unlock the lightweight and multifunctional potential of such architectures in aerospace heat exchangers.

To address these challenges, thermomechanical homogenization has emerged as an effective method to approximate the overall structural and thermal response of complex periodic media through simplified representations [21]. In particular, strain energy–based homogenization techniques provide accurate equivalent stiffness matrices by linking microstructural mechanics to macroscopic responses, while energy-based homogenization for thermal conductivity estimation, consistent with Gibson–Ashby principles, captures anisotropic transport properties without resorting to detailed meshing [22]. These approaches offer significant advantages, as they preserve the essential anisotropy of periodic geometries while drastically reducing computational effort, enabling efficient structural-thermal assessments of intricate architectures such as TPMS lattices [23].

In the context of aircraft applications, where heat exchangers are often inclined within ducts to optimize flow and integration, evaluating structural stresses across inclination angles is critical for predicting performance and fatigue resistance [24]. TPMS-based HEXs, in particular, exhibit unique load paths and stress localization patterns that directly influence their durability under cyclic loads. By integrating homogenized stiffness and conductivity matrices derived from representative volume elements into duct-level models, it becomes possible to capture the stress distributions without full-scale simulations, while still reflecting the anisotropic mechanics of the underlying architecture. This approach not only enhances predictive capability but also supports the development of lightweight, structurally-enhanced multifunctional heat exchangers tailored for aerospace ducts, demonstrating how homogenization bridges microscale design innovation with macroscale structural integrity.

5.1. Stiffness matrix and thermal conductivity matrix assessment

Finite Element (FE) analysis of large arrays of cellular structures is computationally expensive and time-consuming because of the complexity of the geometry. The hybrid cellular designs considered are periodic in all three directions and this allows for characterization of their properties using homogenization methods [22]. The homogenization technique used in this paper is applied to the Representative Volume Element (RVE) of the lattice structure and it is based on the equivalence between the

strain energy of the heterogeneous RVE and that of the equivalent homogeneous anisotropic medium replacing it at the upper scale. The numerical homogenization method presented here is of general nature and can be used to characterize the elastic modulus, shear modulus, bulk modulus, and degree of anisotropy. FE simulations are performed using ANSYS APDL software[5]. The volume fraction of the RVE is defined as $\bar{\rho} = V/V_{\text{RVE}}$, where V is the actual volume occupied by the solid phase, whereas $V_{\text{RVE}} = 8a_1a_2a_3$ is the volume of the parallelepiped (of which the generic edge length is $2a_j, j = 1,2,3$) embedding the lattice RVE. The axis notation used in the subsequent homogenization analysis corresponds to $x = 1, y = 2, z = 3$, where y axis is along the air flow direction as depicted in FIGURE 2.

5.1.1. Stiffness matrix

The macroscopic constitutive relation between stress $\bar{\sigma}$ and strain $\bar{\varepsilon}$ is represented by the following equation (9):

$$\bar{\sigma} = \bar{C}\bar{\varepsilon} \tag{9}$$

where the stress and strain tensors are represented using the Voigt's notation as follows [25]:

$$\bar{\sigma} = \{\bar{\sigma}_{11}\ \bar{\sigma}_{22}\ \bar{\sigma}_{33}\ \bar{\sigma}_{23}\ \bar{\sigma}_{31}\ \bar{\sigma}_{12}\}^{\mathrm{T}}, \tag{10}$$

$$\bar{\varepsilon} = \{\bar{\varepsilon}_{11}\ \bar{\varepsilon}_{22}\ \bar{\varepsilon}_{33}\ 2\bar{\varepsilon}_{23}\ 2\bar{\varepsilon}_{31}\ 2\bar{\varepsilon}_{12}\}^{\mathrm{T}}. \tag{11}$$

In anisotropic cellular structures, the mechanical behavior is governed by the full stiffness tensor $\bar{C}$, which includes nine independent coordinates. $\bar{C}_{11}, \bar{C}_{22}, \bar{C}_{33}$ are the axial stiffnesses in x, y, z directions (effective Young's moduli); $\bar{C}_{12}, \bar{C}_{13}, \bar{C}_{23}$, are the coupling terms, that link stress in one direction to strain in another (Poisson effects, but direction-dependent); $\bar{C}_{44}, \bar{C}_{55}, \bar{C}_{66}$ are shear moduli along the three orthogonal planes.

5.1.2. Thermal conductivity matrix, TCM

The macroscopic constitutive relation between the heat flux $\bar{\mathrm{q}}$ and the temperature gradient $\bar{\mathrm{T}}$ is represented by the following:

$$\bar{\mathrm{q}} = -\bar{\mathrm{k}}\bar{\mathrm{T}} \tag{12}$$

where the heat flux and the temperature gradient vectors are represented using the Voigt's notation as follows [26] [22] [27]:

$$\bar{\mathrm{q}} = \{\bar{\mathrm{q}}_{11}\ \bar{\mathrm{q}}_{22}\ \bar{\mathrm{q}}_{33}\}^{\mathrm{T}}, \tag{13}$$

$$\bar{\mathrm{T}} = \{\bar{\mathrm{T}}_{11}\ \bar{\mathrm{T}}_{22}\ \bar{\mathrm{T}}_{33}\}^{\mathrm{T}}. \tag{14}$$

In anisotropic cellular structures, the thermal conduction behavior is governed by the thermal conductivity tensor $\bar{k}$, which includes six independent coordinates: $\bar{k}_{11}, \bar{k}_{22}, \bar{k}_{33}$, $\bar{k}_{12}, \bar{k}_{13}, \bar{k}_{23}$ .These coordinates define the orthotropic symmetry, capturing the variation of heat transport in each principal direction. For materials with higher symmetry (e.g., cubic or transversely isotropic), the number of independent thermal conductivity coordinates reduces accordingly, and in our case the $\bar{k}_{11}, \bar{k}_{22}, \bar{k}_{33}$ terms are more prominent.

5.2. Numerical homogenization approach

In modeling porous cellular materials, the Gibson-Ashby framework provides a widely accepted methodology for estimating effective macroscopic properties based on micro-structural parameters [22]. This model is developed under three principal assumptions: first, the bulk material constituting the RVE exhibits a linear behavior; second, the buckling of thin walls or struts in the cellular structure is disregarded; and third, the equivalent homogeneous material at the macroscale behaves in accordance with the characteristics of random and symmetric cellular foams.

5.2.1. Strain energy-based homogenization method of periodic media

The strain energy-based homogenization method is a general numerical approach used to estimate the effective mechanical properties of periodic structures and materials. In this technique, an RVE that captures the repeating microstructural pattern is subjected to predefined macroscopic strain fields. The fundamental principle relies on Hill's energy criterion, which states that the volume-averaged microscopic strain energy must equal the macroscopic strain energy for consistency between scales [22] [25]. By applying controlled deformations (such as axial or shear loading) and computing the resulting average stresses, the components of the effective stiffness tensor can be derived. This method is particularly suited for complex architectures like TPMS and strut-based lattices, where direct analytical estimation is difficult, ensuring that the equivalent material properties reflect the true behavior of the periodic microstructure.

Periodic boundary conditions are imposed on the faces, edges, and vertices of the RVE using constraint equations as described below to achieve strain energy-based homogenization. In vector notation, let the RVE be $\Omega = [-a_1, a_1] \times [-a_2, a_2] \times [-a_3, a_3]$ with the side lengths of $L_j = 2a_j$ and unit vectors $e_j (j = 1,2,3)$. It is considered that $u(x) \in \mathbb{R}^3$is the displacement field and $\varepsilon^0 \in \mathbb{R}^{3\times3}$ is the prescribed macroscopic (average) strain tensor (so $\varepsilon^0 d$ is the macroscopic displacement jump produced by a translation d). Points on opposite boundaries are paired by translations built from $L_j e_j$.

Face constraints are applied across opposite faces of the RVE to ensure periodicity as follows, where x lies on the "minus" face normal to e_j and $\mathrm{x} + L_j e_j$ is the matching point on the opposite "plus" face:

$$\mathrm{u}\big(\mathrm{x} + \mathrm{L_j e_j}\big) - \mathrm{u(x)} = \varepsilon^0\big(\mathrm{L_j e_j}\big), \quad \mathrm{x} \in \{\mathrm{x_j} = \mathrm{a_j}\}, \mathrm{j} = 1,2,3 \tag{15}$$

The edge constraints enforce periodicity along the edges formed by the intersection of faces as follows:

$$\mathrm{u}\big(\mathrm{x} + \mathrm{s_j L_j e_j} + \mathrm{s_k L_k e_k}\big) - \mathrm{u(x)} = \varepsilon^0(\mathrm{s_j L_j e_j} + \mathrm{s_k L_k e_k}), \tag{16}$$

where $j \neq k \in \{1,2,3\}, s_j, s_k \in \{\mp 1\}$, and $x \in \{x_j = s_j a_j, x_k = s_k a_k\}$, which helps tie each edge to its opposite edge

[5] ANSYS® Academic Research Mechanical APDL, 2024 R2

via a translation to flip the two involved coordinates. The vertex constraints ensure consistency across diagonally opposite corners of the RVE as follows, with $s_m \in \{\mp 1\}$ and $\mathrm{x} \in \{x_m = -s_m a_m \text{ for } \mathrm{m} = 1,2,3\}$ (a corner).

$$\mathrm{u}\left(\mathrm{x} + \sum_{\mathrm{m}=1}^{3} \mathrm{s_m L_m e_m}\right) - \mathrm{u(x)} = \varepsilon^0 \left(\sum_{\mathrm{m}=1}^{3} \mathrm{s_m L_m e_m}\right), \quad (17)$$

The homogenized stress calculation of average (volume-averaged) stress coordinate $\bar{\sigma}_\alpha$ in Voigt notation, corresponding to an imposed strain $\bar{\varepsilon}^0_\beta$, is computed as:

$$\bar{\sigma}_\alpha\left(\bar{\varepsilon}^0_\beta\right) \approx \frac{1}{\mathrm{V_{RVE}}} \sum_{\mathrm{e}=1}^{\mathrm{N_e}} \sigma_{\alpha \mathrm{e}}\left(\bar{\varepsilon}^0_\beta\right) \cdot \mathrm{V_e} \text{ for } \alpha = 1, \ldots, 6 \quad (18)$$

where, N_e is the total number of finite elements in the RVE mesh, V_e is the volume of the e^{th} element, $\sigma_{\alpha e}$ is the α^{th} stress component in the e^{th} element.

Each component of the homogenized elasticity matrix (for the equivalent anisotropic material) is calculated as:

$$\bar{\mathrm{C}}_{\alpha\beta} = \frac{\bar{\sigma}_\alpha\left(\bar{\varepsilon}^0_\beta\right)}{\bar{\varepsilon}^0_\beta} \text{ for } \alpha, \beta = 1, \ldots, 6 \quad (19)$$

This approach forms the basis of numerical homogenization using strain energy equivalence and periodic boundary conditions. Barbero et al [25] explains the theoretical concepts pertaining to computational homogenization in periodic media.

5.2.2. Energy-based homogenization method for thermal conductivity estimation

The energy-based homogenization method is a widely used numerical approach for estimating the effective thermal conductivity tensor of periodic heterogeneous cellular materials. Analogous to mechanical homogenization, this method relies on the equivalence of microscopic and macroscopic heat conduction behavior to ensure scale consistency. In this approach, the RVE that encapsulates the periodic thermal features of the material is subjected to predefined macroscopic temperature gradients. The core principle is based on the equivalence of thermal energy dissipation, which ensures that the volume-averaged microscopic heat flux corresponds to the effective macroscopic heat flux resulting from the same imposed gradient [25]. Controlled unit gradients are applied in the principal directions, and the resulting average heat fluxes are computed over the volume of the RVE. These calculations enable the determination of the components of the effective thermal conductivity tensor $\bar{k}^0_{ij}$.

Periodic boundary conditions are imposed to enforce temperature difference across opposing faces to match the prescribed macroscopic gradient, whilst maintaining a periodic heat flux.

$$\begin{aligned} \mathrm{T_i}(\mathrm{a_1}, \mathrm{x_2}, \mathrm{x_3}) - \mathrm{T_i}(-\mathrm{a_1}, \mathrm{x_2}, \mathrm{x_3}) &= 2\mathrm{a_1}\bar{\mathrm{k}}^0_{\mathrm{i1}} \\ \mathrm{T_i}(\mathrm{x_1}, \mathrm{a_2}, \mathrm{x_3}) - \mathrm{T_i}(\mathrm{x_1}, -\mathrm{a_2}, \mathrm{x_3}) &= 2\mathrm{a_2}\bar{\mathrm{k}}^0_{\mathrm{i2}} \\ \mathrm{T_i}(\mathrm{x_1}, \mathrm{x_2}, \mathrm{a_3}) - \mathrm{T_i}(\mathrm{x_1}, \mathrm{x_2}, -\mathrm{a_3}) &= 2\mathrm{a_3}\bar{\mathrm{k}}^0_{\mathrm{i3}} \end{aligned} \quad (20)$$

In the above equations, T_i is the temperature field and $\bar{k}^0_{ij}$ is the applied macroscopic temperature gradient. The average heat flux $\bar{T}_i$ in the i direction for each imposed temperature gradient direction $\bar{T}_j$ is estimated as:

$$\bar{\mathrm{q}}_\mathrm{i} = \frac{1}{\mathrm{V_{RVE}}} \sum_{\mathrm{e}=1}^{\mathrm{N_e}} \mathrm{q_{i,e}} \cdot \mathrm{V_e} \quad (21)$$

Where $\bar{q}_i$ is the i^{th} component of the macroscopic heat flux vector, $q_{i,e}$ is the i^{th} component of the microscopic heat flux in element e, N_e is the total number of finite elements in the RVE mesh, and V_e is the volume of the e^{th} element. Each component of the homogenized thermal conductivity tensor $\bar{k}^0_{ij}$ is obtained using the relation $\bar{k}^0_{ij} = -\bar{q}_i/\bar{T}_j$,for $i, j = 1,2,3$.

6. STRUCTURAL ASSESSMENT RESULTS

This chapter applies the aforementioned methodology to the gyroid-pipe AR1, AR1.5, and AR2 unit cell geometries. The results of the matrix assessment of their stiffness and thermal conductivity are described. The second chapter includes an additional study that quantifies the stress-strain results of the AR1, AR1.5, and AR2 in different inclined positions inside a generic nacelle domain. These results will be used in a later design phase to study HEX integrations inside the propulsion system domain.

6.1. Stiffness matrix and thermal conductivity matrix assessment

The homogenized results of the stiffness matrix in GPa and TCM in $W/m.K$ are illustrated in FIGURE 7. The C11 value for AR2 is observed to be 41% lower and for AR1.5 is 26% lower compared to AR1, indicating a substantial reduction in stiffness along the x-direction as the aspect ratio increases. Similarly, the C33 value of AR2 is 25% less than that of AR1 and 15% less than AR1.5, reflecting a decline in stiffness along the z-direction with increasing aspect ratio. In contrast, C22 for AR2 is 13% greater than for AR1.5 and 37% greater than for AR1, suggesting enhanced stiffness along the y-direction for AR2. The elastic constants C12, C13, C23, C44, and C66 remain approximately constant across all three geometries, indicating that these parameters are largely unaffected by changes in aspect ratio. The C55 value for AR1 is 22% greater than that of AR2 and 14% greater than AR1.5. This is mainly due to shift in structural mass along the y-direction. Regarding thermal conductivity coefficients, both TCM11 and TCM33 decrease progressively from AR1 to AR2, while TCM22 for AR2 is 18% higher than for AR1 and 6% higher than for AR1.5. This increment is caused majorly due to increment in heat transfer surface area along the x-direction. As explained in chapter 2 and in TAB 1, the porosity of the AR1, AR1.5 and AR2 remains same at 62% as the void volume fraction. This means 62% of the RVE consists of fluid region.

6.2. Variation of stress-strain results in accordance with inclination

Understanding structural performance at different inclinations is essential because lattice load paths, bending–axial mix, and effective stiffness all change with orientation. These changes can alter the location of peaks stresses and strains occur under service loads. Zhang et al [28] has investigated the CFD performance of TPMS geometries for different rotating angles but not investigated the mechanical performances. This paper uses the earlier-

identified anisotropic stiffness matrices to project the material response into different angles of inclination relative to the airflow direction, shown in FIGURE 8. The cross-section of each panel is 200 mm x 200 mm, and the respective lengths (thickness of HEX segments) are listed in TAB 2. The panel's external edges are all constrained by fixed boundary conditions, which represent its clamped installation and prevent rigid-body motion. Rather than being sharp, geometric edges are filleted to eliminate artificial stress singularities and produce realistic stress distributions that reflect manufacturable features. Prior to the final runs, a mesh-convergence study is completed; the selected mesh size is the coarsest that reproduced stable peak stress and strain metrics within a predefined tolerance, ensuring accuracy without unnecessary computational cost.

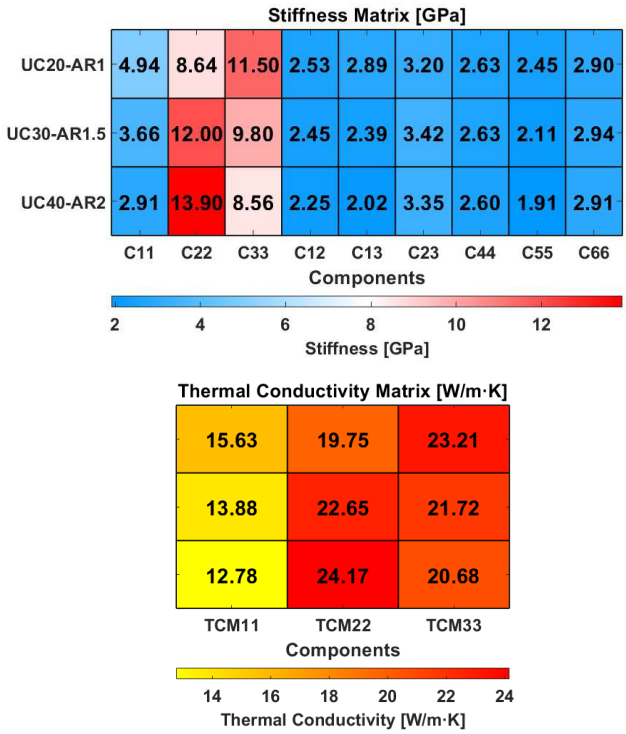

FIGURE 7 Stiffness matrix (top) and thermal conductivity matrix (bottom) results.

To represent the operating conditions, pressure and thermal loads obtained from CFD simulations are applied on the HEX surfaces. Thermal loads are found to dominate the structural response, while pressure loads had a comparatively minor influence. Consequently, detailed variations in pressure drop with angle of attack at the inlet are disregarded, and a uniform pressure drop is assumed across all inclinations of a given configuration. Additionally, external structural loads and vibrational effects are excluded because the objective of this study is to conduct a comparative analysis of various configurations under consistent thermal-pressure boundary conditions.

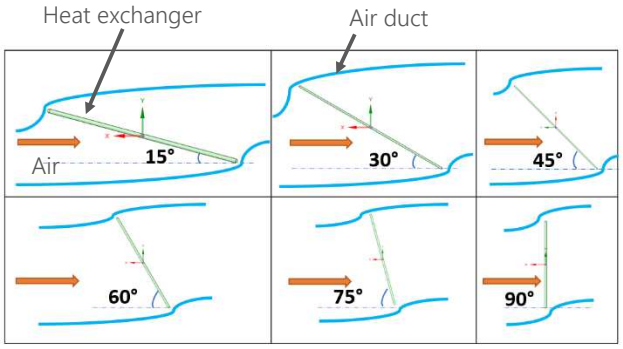

FIGURE 8 Different HEX inclinations inside a generic duct.

TAB 3 contains the variation of the maximum equivalent Von-Mises stresses with the inclination of the HEX. The individual ARs cases of the gyroid-pipe AR1, AR1.5, and AR2 show clear differences in their angular response. AR2 reaches its maximum stress of 46.4 MPa at 15°, then steadily declines to 19.1 MPa at 90°, demonstrating the steepest drop among the three cases. AR1.5 begins at 29.4 MPa at 15°, peaks at around 28.6 MPa at 30°, and falls to 15.4 MPa at 90°, showing a moderate decline. In contrast, AR1 remains relatively stable, ranging from 17.3 MPa at 15° down to 15.0 MPa at 90°, indicating the least sensitivity to angular changes among all the configurations. These results indicates that individual aspect ratio cases of the gyroid-pipe AR1, AR1.5, and AR2 exhibit the highest stresses at 15°. These subsequently decreases with an increase in inclination until 90° under the same set of loading criteria, indicating favorable structural behavior at higher inclinations. It should also be noted that higher aspect ratios initially exhibit high stresses but become more prone to reductions as inclination increases. In contrast, AR1 maintains a consistent, but lower, stress performance.

The configurations with combined ARs, listed in TAB 2, exhibit distinct peak behaviors. For example, AR1.5-AR2, AR2-AR1.5, AR2-AR1 and AR1-AR2 exhibit stresses above 60 MPa across most angles, with peaks of 65.6 MPa, 67.8 MPa at 45°, 80.6 MPa, 77.8 MPa at an angle of 45° respectively. These values start tapering down and tend to reach a minimum at 75° for or at 90°. These hybrid cases exhibit lower stresses at lower and higher inclination angles making them favorable design selections for these angles. The AR1-AR1.5 and AR1.5-AR1 cases reach around 44–54 MPa, with peaks near 45° that tapes down at higher angles. The three-way combination AR1-AR1.5-AR2 reaches 51.9 MPa at 45°, dropping to 39.7 MPa at 90°, while AR2-AR1.5-AR1 follows a similar trend with 45.0 MPa at 45° and 35.6 MPa at 90°.

These results suggest that triple combinations of ARs offer a more balanced angular response and exhibit less stress than dual combinations of ARs. Overall, the analysis shows that AR1, AR1.5, and AR2 are favorable design selections for higher inclinations, while combined HEX segments are good selections for lower and higher inclinations. This assessment demonstrates the effectiveness of the homogenization approach for quickly evaluating the stresses experienced by AR design combinations and their performance.

Configuration	L	Angle of inclination					
Unit	mm	15°	30°	45°	60°	75°	90°
AR1	20	17.3	17.6	16.8	16.0	15.6	15.0
AR1.5	30	29.4	28.6	26.9	21.6	15.1	15.4
AR2	40	46.4	40.0	36.9	33.2	27.4	19.1
AR1-AR1.5	50	35.4	42.3	44.5	42.6	47.1	44.2
AR1.5-AR1	50	42.8	50.5	54.0	52.9	39.4	45.5
AR1.5-AR2	70	51.3	61.8	65.6	61.6	57.1	53.7
AR2-AR1.5	70	57.4	63.2	67.8	61.8	63.9	53.9
AR1-AR2	60	50.7	64.4	77.8	75.4	57.0	49.7
AR2-AR1	60	53.0	66.1	80.6	67.5	57.2	54.1
AR1-AR1.5-AR2	90	33.7	37.9	51.9	47.1	42.5	39.7
AR2-AR1.5-AR1	90	37.4	37.9	45.0	38.6	47.7	35.6

TAB 3 Maximum equivalent Von-Mieses stresses in [MPa].

7. SUMMARY AND CONCLUSION

This paper addresses the technical challenge of increasing the power density of a fuel cell-powered all-electric aircraft propulsion system and deals with the design development of compact heat exchangers. It presents the design and performance assessment of a novel, gyroid-based TPMS HEX and introduces the integration of coolant channels inside gyroid surfaces. To estimate performance, small repeating periodic cells with three different aspect ratios (AR1, AR1.5, and AR2) are designed, stretching their lengths along the air side by factors of 1, 1.5, and 2, respectively with respect to their width. CFD simulations are performed to evaluate the thermal-hydraulic coupling of the conjugated heat transfer. The results show that the combined performance improves with higher ARs because, with stretched designs, the pressure loss along the air side decreases more than their heat transfer capability. In addition to AR1, AR1.5, and AR2, eight different combinations are configured, and the pressure drop across the air side is measured experimentally. Verifying the CFD results, it is found that higher ARs deliver lower pressure drop and, consequently, lower pumping power penalty. According to the test data, the AR2-AR1.5 configuration delivers 3% less pumping power while increasing the heat transfer surface area 3.12 times relative to the AR1 configuration, without changing the frontal area or mass flow rate. This makes it a potential candidate for future studies involving thermal testing to validate thermal-hydraulic coupled performance.

Structural analysis of gyroid-pipe HEX includes two complementary evaluations: a theoretical assessment of stiffness and thermal conductivity matrices, and a structural assessment of stresses under different inclinations inside the air duct. The stiffness and conductivity results confirmed anisotropy, showing directional behavior of AR variation. The stress analysis shows that AR1 and AR1.5 are favorable single cases at high inclinations, whereas combinations of all three segments provide the most angle-resilient and efficient option overall.

In the near future, parametric design optimization will be used to determine the limits of changes in the gyroid aspect ratio, wall thickness and orientation of the coolant channels on the thermal-hydraulic performance. Validation of the thermal performance is planned using experiments with printed metal HEX segments. Additionally, the AR2-AR1.5 combination is to be tested at various air and coolant flow rates and temperatures. The effect of inclined HEX segments inside air ducts on thermal-hydraulic performance is a research goal for the near future. Furthermore, structural tests must be conducted to validate FE simulations, with the aim of including dynamic loads and vibration tests.

REFERENCES

[1] Clean Sky 2 Joint Undertaking, *Hydrogen-powered aviation. A fact-based study of hydrogen technology, economics, and climate impact by 2050*, Publications Office of the European Union, Luxembourg, May 2020.

[2] Hepperle, M., "Electric Flight – Potential and Limitations," [online], 2012, https://elib.dlr.de/78726/1/MP-AVT-209-09.pdf.

[3] Alteneiji, M., Ali, M. I. H., Khan, K. A., and Al-Rub, R. K. A., "Heat transfer effectiveness characteristics maps for additively manufactured TPMS compact heat exchangers," *Energy Storage and Saving*; Vol. 1, No. 3, 2022, pp. 153–161. doi: 10.1016/j.enss.2022.04.005.

[4] Yeranee, K., and Rao, Y., "A Review of Recent Investigations on Flow and Heat Transfer Enhancement in Cooling Channels Embedded with Triply Periodic Minimal Surfaces (TPMS)," *Energies*; Vol. 15, No. 23, 2022, p. 8994. doi: 10.3390/en15238994.

[5] Kays, W. M., and London, A. L., "Compact Heat Exchangers," 2018.

[6] Schmelcher, M., and Hässy, J., "Hydrogen fuel cells for aviation: A potential analysis comparing different thrust categories," [online], ISABE_2022_291, 2022, ISABE.

[7] Li, W., Yu, G., and Yu, Z., "Bioinspired heat exchangers based on triply periodic minimal surfaces for supercritical CO2 cycles," *Applied Thermal Engineering*; Vol. 179, 2020, p. 115686. doi: 10.1016/j.applthermaleng.2020.115686.

[8] Thomas, N., Sreedhar, N., Al-Ketan, O., Rowshan, R., Abu Al-Rub, R. K., and Arafat, H., "3D printed triply periodic minimal surfaces as spacers for enhanced heat and mass transfer in membrane distillation," *Desalination*; Vol. 443, 2018, pp. 256–271. doi: 10.1016/j.desal.2018.06.009.

[9] Iyer, J., Moore, T., Du Nguyen, Roy, P., and Stolaroff, J., "Heat transfer and pressure drop characteristics of heat exchangers based on triply periodic minimal and periodic nodal surfaces," *Applied Thermal Engineering*; Vol. 209, 2022, p. 118192. doi: 10.1016/j.applthermaleng.2022.118192.

[10] Femmer, T., Kuehne, A. J., and Wessling, M., "Estimation of the structure dependent performance of 3-D rapid prototyped membranes," *Chemical Engineering Journal*; Vol. 273, 2015, pp. 438–445. doi: 10.1016/j.cej.2015.03.029.

[11] Kim, J., and Yoo, D.-J., "3D printed compact heat exchangers with mathematically defined core

structures," *Journal of Computational Design and Engineering*; Vol. 7, No. 4, 2020, pp. 527–550. doi: 10.1093/jcde/qwaa032.

[12] Dixit, T., Al-Hajri, E., Paul, M. C., Nithiarasu, P., and Kumar, S., "High performance, microarchitected, compact heat exchanger enabled by 3D printing," *Applied Thermal Engineering*; Vol. 210, 2022, p. 118339. doi: 10.1016/j.applthermaleng.2022.118339.

[13] Bhapkar, S., Sain, C., and Kazula, S., "Design of Heat Exchangers with Cooling Fins in Fuel Cell-Powered Electric Aircraft: Genetic Optimization Approach with CFD Validation," *2025 IEEE/AIAA Transportation Electrification Conference and Electric Aircraft Technologies Symposium (ITEC+EATS),* IEEE, 2025, pp. 1–8.

[14] Sain, C. K., and Kazula, S., "Comparative Assessment of Compact Air Heat Exchangers for Fuel Cell-Powered Electric Aircraft," *AIAA AVIATION FORUM AND ASCEND 2024,* American Institute of Aeronautics and Astronautics, Reston, Virginia, 2024.

[15] Liu, J., Cheng, D., Oo, K., Pan, W., McCrimmon, T.-L., and Bai, S., "Optimization of Triply Periodic Minimal Surface Heat Exchanger to Achieve Compactness, High Efficiency, and Low-Pressure Drop," *Energies*; Vol. 17, No. 20, 2024, p. 5141. doi: 10.3390/en17205141.

[16] Gajetti, E., Boccardo, G., Savoldi, L., and Marocco, L., "Hydrodynamic characterization of Gyroid, Diamond and Split-P Triply Periodic Minimal Surfaces as porous medium," *International Journal of Heat and Mass Transfer*; Vol. 252, 2025, p. 127439. doi: 10.1016/j.ijheatmasstransfer.2025.127439.

[17] Manglik, R. M., and Bergles, A. E., "Heat transfer and pressure drop correlations for the rectangular offset strip fin compact heat exchanger," *Experimental Thermal and Fluid Science*; Vol. 10, No. 2, 1995, pp. 171–180. doi: 10.1016/0894-1777(94)00096-Q.

[18] Singh, K. P., and Soler, A. I., *Mechanical Design of Heat Exchangers*, Springer Berlin Heidelberg, Berlin, Heidelberg, 1984.

[19] Asli, M., König, P., Sharma, D., Pontika, E., Huete, J., Konda, K. R., Mathiazhagan, A., Xie, T., Höschler, K., and Laskaridis, P., "Thermal management challenges in hybrid-electric propulsion aircraft," *Progress in Aerospace Sciences*; Vol. 144, 2024, p. 100967. doi: 10.1016/j.paerosci.2023.100967.

[20] Hanks, B., Berthel, J., Frecker, M., and Simpson, T. W., "Mechanical properties of additively manufactured metal lattice structures: Data review and design interface," *Additive Manufacturing*; Vol. 35, 2020, p. 101301. doi: 10.1016/j.addma.2020.101301.

[21] Garnier, C., Vincent, S., Lamagnere, P., Lejeail, Y., and Cachon, L., "Thermo-Mechanical Calculation of Printed Circuit Heat Exchanger Using Homogenization," *Journal of Thermal Science*; Vol. 31, No. 6, 2022, pp. 2309–2328. doi: 10.1007/s11630-022-1646-1.

[22] Gibson, L. J., and Ashby, M. F., "The mechanics of three-dimensional cellular materials," *Proceedings of the Royal Society of London. A. Mathematical and Physical Sciences*; Vol. 382, No. 1782, 1982, pp. 43–59. doi: 10.1098/rspa.1982.0088.

[23] Rishmany, J., Mabru, C., Chieragatti, R., and Rezaï Aria, F., "Simplified modelling of the behaviour of 3D-periodic structures such as aircraft heat exchangers," *International Journal of Mechanical Sciences*; Vol. 50, No. 6, 2008, pp. 1114–1122. doi: 10.1016/j.ijmecsci.2008.01.006.

[24] Singh, A., Jaber, A., and Karathanasopoulos, N., "Fatigue performance of TPMS-based AlSi10Mg architected cellular materials fabricated via hybrid and powder bed fusion methods," *International Journal of Fatigue*; Vol. 193, 2025, p. 108758. doi: 10.1016/j.ijfatigue.2024.108758.

[25] Barbero, E. J., *Introduction to composite materials design*, Taylor & Francis CRC Press, Boca Raton, 2018.

[26] Otero, F., Oller, S., Martinez, X., and Salomón, O., "Numerical homogenization for composite materials analysis. Comparison with other micro mechanical formulations," *Composite Structures*; Vol. 122, 2015, pp. 405–416. doi: 10.1016/j.compstruct.2014.11.041.

[27] Mathiazhagan, A., Rincaweski Vegini, G. L., Höschler, K., Montemurro, M., Asli, M., and Reddy Konda, K., "Analysis of Additively Manufactured Cellular Structures As Heat Exchangers for Lightweight Designs in Electrified Propulsion Systems," *Volume 8: Structures and Dynamics — Bearing & Seal Dynamics; Emerging Methods in Engineering Design, Analysis and Additive Manufacturing; Fatigue, Fracture & Life Prediction; Probabilistic Methods; Rotordynamics,* American Society of Mechanical Engineers, 2025.

[28] Zhang, T., Liu, F., Zhang, K., Zhao, M., Zhou, H., and Zhang, D. Z., "Numerical study on the anisotropy in thermo-fluid behavior of triply periodic minimal surfaces (TPMS)," *International Journal of Heat and Mass Transfer*; Vol. 215, 2023, p. 124541. doi: 10.1016/j.ijheatmasstransfer.2023.124541.